Chemosphere 370 (2025) 143971

Contents lists available at ScienceDirect

Chemosphere

journal homepage: www.elsevier.com/locate/chemosphere

Novel S-scheme based nanocomposite of MXene/V_2O_5 for environmental remediation towards sustainable development: An insight into influencing parameters

Nahid Tyagi [a,b,c], Diksha Sharma [b], Manika Khanuja [b,*]

[a] Department of Physics and Astrophysics, Central University of Haryana, Mahendragarh, 123031, India
[b] Centre for Nanoscience and Nanotechnology, Jamia Millia Islamia, New Delhi, 110025, India
[c] Dr. Bansi Dhar Institute, Gurugram, 122007, India

HIGHLIGHTS

- Novel heterostructure of MXene/V_2O_5 was efficiently synthesized via ball milling and hydrothermal approach.
- Heterostructures are highly efficient to fulfil SDG goal 14 and 7, Save Lives Below Water and Water for All.
- Removal efficiency enhanced approx. two-fold in case of MV nanocomposite as compared pristine samples.
- S-scheme based heterostructures shows highly efficient CV removal performance and reuse convenience.
- Enhanced degradation was explained on the basis of Zeta, EIS, Mott-Schottky and EPR analysis.

GRAPHICAL ABSTRACT

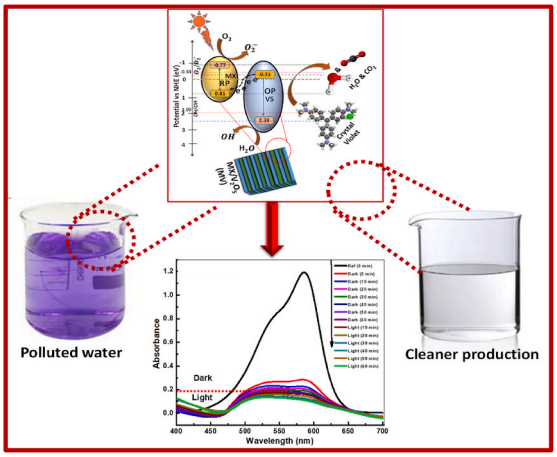

ARTICLE INFO

Handling editor: Jun Huang

Keywords:
MXene/V_2O_5 nanocomposite
Textile dyes
Photocatalysis
S-Scheme
EPR and trapping study

ABSTRACT

In this study, a novel 2D/2D nanocomposite of MXene and V_2O_5 was synthesized using a facile hydrothermal approach for the efficient removal of crystal violet (CV), a textile dye from contaminated water to achieve Sustainable Development Goal (SDG) 14; "Save Lives Below Water". Here, the catalytic performance of pristine MXene was prominently boosted with the introduction of ball milled V_2O_5 as an electron generating agent. The degradation efficiency of synthesized nanocomposite significantly enhanced from 57 % to 92 %, 41 % – 76 % and 7 % – 58 % with an error of ±2 % as compared to pristine MXene at 10, 20 and 30 ppm concentrations of CV, respectively. The effective degradation of pollutants is ascribed to the electron-transfer via S-scheme based mechanism and helps in reducing recombination rate of photogenerated carriers, which could produce hydroxyl radicals ($OH^{\cdot}$) as a primary species for effectively degradation of pollutants.

* Corresponding author.
E-mail address: manikakhanuja@gmail.com (M. Khanuja).

https://doi.org/10.1016/j.chemosphere.2024.143971
Received 1 August 2024; Received in revised form 28 November 2024; Accepted 14 December 2024
Available online 21 December 2024
0045-6535/© 2024 Elsevier Ltd. All rights are reserved, including those for text and data mining, AI training, and similar technologies.

The superior performance of nanocomposite is attributed to: (i) the optimized surface charge (−27.8 mV), (ii) small value of charge transfer resistance (R_{ct} = 1.3 Ω), (iii) enhanced value of carrier concentration (6.3 X 10^{32} cm^{-3}), (iv) small recombination rate of excitons and (v) high specific surface area as compared to pristine samples. Moreover, to strengthen the findings, scavenger study and electron paramagnetic resonance (EPR) study were carried out and concluded that hydroxyl radicals ($OH^{\cdot}$) are the primary species in the mineralization of CV dye. The values of lande g-factor are calculated using EPR plots which comes out to be 2.03 and 2.04 for (O_2^{-}) and ($OH^{\cdot}$) radicals, respectively and demonstrates the formation of free radicals during catalytic reactions. The Chemical Oxygen Demand (COD) analysis was carried out before and after the removal of CV using MV nanocomposite and confirms the reduction in COD vlaue of 81.60 %. The reusability experiment confirms stability of synthesized sample and provides a good shred for industrial applications in the treatment of wastewater and getting out cleaner productions and to save marine ecosystem.

1. Introduction

Colors and dyes have an adverse effect on marine life and can change many aspects of ocean ecosystems. Numerous colors and dyes used in the paper, leather, and textile industries contain compounds that are toxic for marine life. These colors can contaminate marine life, causing disease, problems with reproduction, and even death, when they are discharged into the water by inappropriate waste disposal or industrial discharge (Mani and Bharagava, 2018; Tkaczyk et al., 2020; Cheng et al., 2021; Sharma et al., 2021; Ramzan et al., 2022). The total population of marine organisms is difficult to quantify accurately, but it is likely to be comparable to or even higher than the total population of organisms on land in terms of biomass and diversity. Researchers are mainly focusing on the prevention of organism/life on land and very few studies have been done in order to save lives below water (Bojarczuk et al., 2018; Khan et al., 2022). Therefore, the authors' goal in this work is to eliminate colors from the oceans and the sea ecology.

Marine ecosystems can be disturbed by dyes because they can change the chemical and physical characteristics of fresh water resources. Certain dyes, for instance, might make water less transparent and light-piercing, which can hinder marine plants' ability to photo-synthesize and have an impact on the development of algae and other primary producers (Dunne et al., 2002; Würth et al., 2013; Kim et al., 2023).

Henceforth, to overcome all these challenges for marine life and ecosystem United Nations Conference on Sustainable Development in Rio de Janeiro in 2012 made Sustainable Development Goal (SDG) 14, which stands for "Save Lives Below Water", aims to conserve and sustainably use the oceans, seas, and marine resources for sustainable development (Cormier and Elliott, 2017; Vadrot, 2023). Out of large range of toxic pollutants which are discharged into water resources, textile dyes are more toxic, carcinogenic, and non-biodegradable in nature (Roy Choudhury, 2014; Maheshwari et al., 2021). The contaminated matrix of textile dyes in the water stream reduce the penetration of sunlight, results in disruption of the biological process and creates worse situation for the aquatic environment and aquatic lives (Gita et al., 2017; Mehra et al., 2021; Islam et al., 2023). Crystal violet (CV), a synthetic and cationic triphenylmethane dye with the chemical formula $C_{25}N_3H_{30}Cl$, is one of the many textile dyes which is widely utilized in the textile and pharmaceutical industries. It is much more complex, carcinogenic in nature, and potentially toxic to mucosal membrane. The complex nature of CV helps it to sustain against light and diversified oxidizing agents. The long-term use of CV dye leads to genetic mutations in living organisms (Zehra et al., 2023).

Such issues have led to the need of scientific as well as technological advancements among the research communities to find answers to the problem of pollution and innovate sustainable methods to achieve the goal of degradation or complete elimination of environmental pollutants.

To quest all these issues, photocatalysis has emerged as an eco-friendly technique for the removal of various types of contaminants from industrial wastewater. Wastewater treatment through photocatalysis is ensued via a set of simultaneous redox chemical reactions based on the generation of reactive oxygen species (ROS) (Allen et al., 2008; Yoon et al., 2010; Loeb et al., 2018; Mittal et al., 2024). Photocatalytic process, utilizes sunlight via a photocatalyst for the degradation of pollutants. The process is based on the oxidation of the pollutant by molecular oxygen, ozone, and hydrogen peroxide under the influence of artificial UV light or sunlight in the presence of dissolved, suspended or immobilized photocatalysts (Kumar et al., 2020, 2022). The photocatalytic degradation of pollutants and waste-water treatment has become a highly coveted research area owing to its advantages over other traditional water purification methods, such as its greater simplicity, efficiency, absence of secondary waste products and the usage of solar radiation for its energy requirement (Spasiano et al., 2015; Baynosa et al., 2020; Tyagi et al., 2023a, 2023c, 2023d).

In previous reported works, mainly photocatalytic performance for the removal of pollutants from wastewater was explained on the basis of type II heterojunction and Z-schemes (Xu et al., 2018; Cai et al., 2019; Mittal et al., 2024). Regrettably, these methods have some constraints pertaining to thermodynamic and kinetic plans, which consequently diminish the photocatalyst's ability to act as an oxidant or a reductant (Wang et al., 2020; Ashraf et al., 2022). Subsequently, Fu et al. (2019) research group has developed a new heterojunction scheme called step-scheme, or "S-scheme" to overcome these shortcomings (Fu et al., 2019).

Briefly, S-scheme heterojunction contains two n-type semiconductors where the one with high conduction band (CB) energy is viewed as reduction photocatalyst (RP) and the other as oxidation photocatalyst (OP). Electrons in the OP's CB were transferred to the RP's VB for recombination upon radiation. In the meantime, holes in VB of OP and electrons collected in CB of RP, both possessing a high redox potential, were primarily accessible for redox processes. Hence, the photocatalytic efficiency has enhanced more strikingly in S-scheme mechanism as compared to other schemes of photocatalytic mechanisms for the removal of noxious pollutants from wastewater.

Recently, MXene a rather new family of 2D material have gained immense attention among various researchers' groups for applications among numerous disciplines such as energy storage, photocatalysis, sensors, electromagnetic applications, biomedical and various other fields (Chen et al., 2020; Lei et al., 2022; Sivasankarapillai et al., 2022; Tyagi et al., 2023b, 2024b). Among the various classes of MXene, Ti_3C_2Tx MXene has emerged as a subject of intense study due to its extremely attractive properties such its large surface area, hydrophilic nature and active surface group terminations which provides it the ability for effective adsorption of pollutants and formation of heterostructures with other semiconductor photocatalysts, flexible layer spacing and exposed active sites on their surface for enhanced trapping of contaminants, strong redox activity, and high conductivity or easier charge transfer mechanism (Pei et al., 2021; Soni et al., 2022; Sadanandan et al., 2023). After possessing of such excellent qualities, it faces some major limitations namely: severe agglomeration and self-stacking of nanosheets results in the opposition to charge transfer and hinder the active sites (Pei et al., 2021; Yu et al., 2021; Sharma et al., 2023). These issues can be resolved by addition of different materials/compounds to

the MXene nanosheets to improvise the interlayer structure (Tyagi et al., 2024a, 2024c).

Vanadium pentoxide (V_2O_5) can be an efficient and promising material for overcoming the issues related to MXene, due to its fabulous physicochemical properties. It is n-type semiconducting material owing to its property of tunable bandgap of around 2.2–2.8 eV in the visible-light region, high chemical activity, photostability and non-toxicity (Sadeghzadeh-Attar, 2020; Kumawat et al., 2021; Bansal et al., 2023).

In this research work, novel hybrid nanocomposite of MXene ($Ti_3C_2T_x$) and V_2O_5 (MV) has been efficiently synthesized for the removal of crystal violet (CV) from wastewater via S-scheme based degradation mechanism. Despite, the fact that many researchers have reported the degradation of CV, but did not get satisfactory results up to higher concentration in wastewater. Herein, photocatalytic degradation of CV up to 30 ppm of water has been efficiently and successfully achieved and studied thoroughly. The synthesized MV nanocomposite proven as the best material for the degradation of CV and can be collected and reused again with efficient stability.

2. Materials and methods

2.1. Materials used

Ammonium fluoride (NH_4F) with purity of 98 % and molecular weight of 37.03 g/mol, titanium aluminum carbide (Ti_3AlC_2) with purity of 99 % and molecular weight of 194.60 g/mol and bulk vanadium pentoxide (V_2O_5) having purity of 98 % and molecular weight of 181.88 g/mol all three chemicals were purchased from Sigma Aldrich and used as bought without further purification. Crystal violet (CV) dye was purchased from Central Drug House (CDH) Pvt. Limited, India.

2.2. Synthesis

The schematic illustrating for the synthesis process of V_2O_5 nanosheets is as shown in Fig. 1 (Scheme 1). First, commercially available 5 g of bulk V_2O_5 powder was taken and transferred in a milling jar having chromium steel balls (5 mm radius), weighing 20.0 g. Another jar was also filled with same amount of sample, and ethanol (30 mL) was added to both the jars as a process controlling agent, to avoid contamination due to wear and tear, as well as to prevent agglomeration. Then, both the jars were placed diametrically opposite to each other in a planetary ball mill (Torrey Hills ND4L). The milling process was taken out at room temperature with a milling rate of 364 rpm, for 24 h. The resulting suspension after the whole run time was separated from the grinding balls using a pipette. The solution was then washed using ethanol and deionized (DI) water via vacuum filtration unit and was then allowed to dry in a vacuum oven at 50 °C for a period of 24 h. Afterward, dried sample was grinded for 45 min to get the final product and labelled as V5.

The synthesis of the nanocomposite was carried out through the addition of pre-synthesized V_2O_5 nanoparticles to the MXene synthesis as shown in Fig. 1(scheme 2). Initially, ammonium fluoride (5.0 g) was dissolved in 60 mL of deionized (DI) water under vigorous stirring for about 10 min. Then, titanium aluminum carbide (0.50 g) was added to ammonium fluoride solution followed by stirring for 5 h, resulting in a black colored solution. Simultaneously, pre-synthesized V_2O_5 nanoparticles was ultrasonicated in 100 mL of DI water, and then added dropwise to the MXene solution. This final solution was subjected to additional stirring for 3 h. The obtained suspension was then transferred into a Teflon-lined hydrothermal autoclave for 36 h at a temperature of 150 °C. The resulting suspension was washed with aqueous solution of NaOH (1 M) and DI water followed by vacuum filtration. The obtained precipitate was allowed to dry overnight in a muffle furnace at 50 °C of temperature and followed by grinding. The resulting fine dark green colored powder was stored in an air proof vial and labelled as MV nanocomposite.

2.3. Characterizations

The morphological details of as-synthesized samples were analyzed

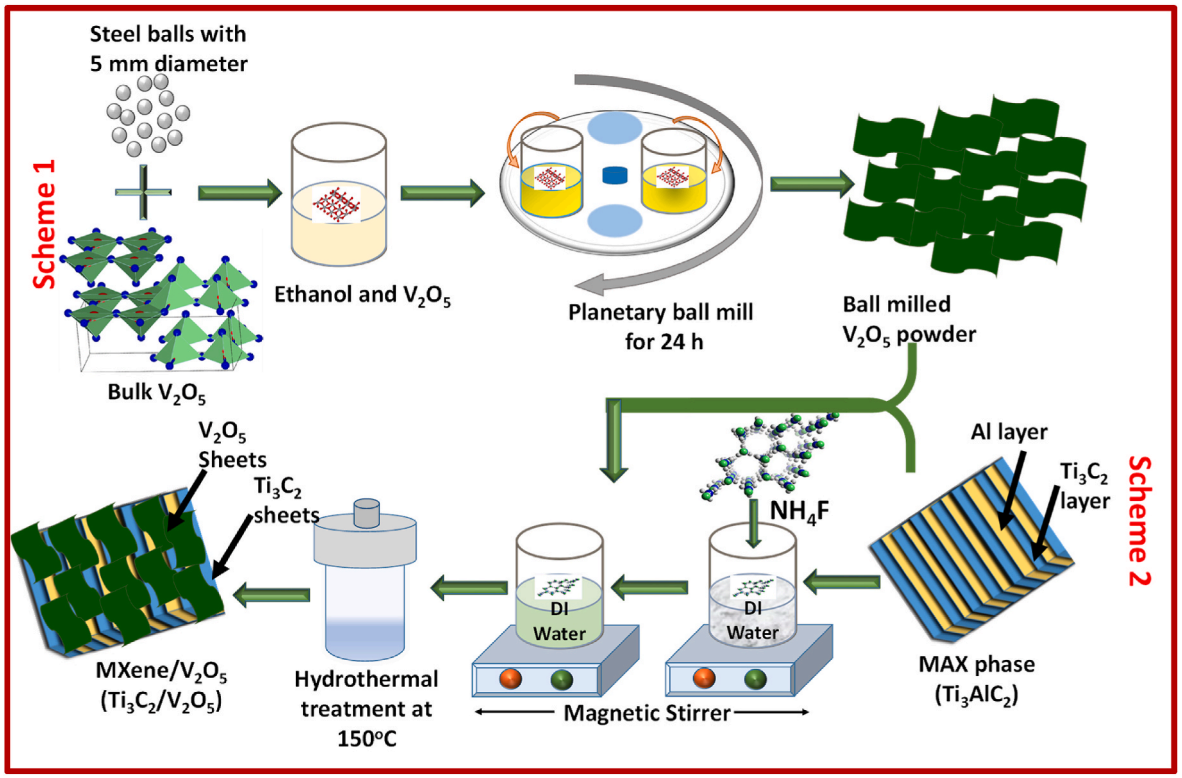

Fig. 1. Schematic for the synthesis of (Scheme 1) V_2O_5 with ball milling technique and (scheme 2) MV (MXene/V_2O_5) nanocomposite using hydrothermal method.

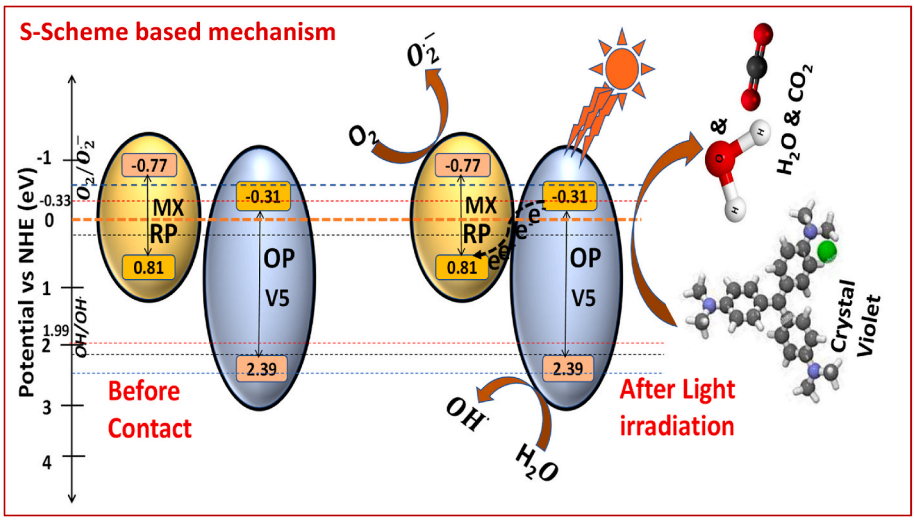

Scheme 1. S-scheme mechanism for the photocatalytic degradation of CV using synthesized MV nanocomposite, before and after contact [MX works as reduction photocatalyst (RP) and V5 works as oxidation photocatalyst (OP)].

using field emission scanning electron microscopy (FESEM) from the Quanta 3D and high-resolution transmission electron microscopy (HRTEM) with model TECNAI 200 kV. X-ray Diffractometer (XRD) was used for the analysis of crystallinity of samples in the range of 10^o-70^o from Rigaku smart lab. For the analysis of functional groups, Fourier Transform Infrared (FTIR) spectroscopy was used from the Bruker tensor 37 spectrometer in the range of 500–4000 cm^{-1}. Optical properties and absorbance spectra of the prepared samples were analyzed using a UV–Vis spectrophotometer of Agilent technology. The elemental composition of the prepared samples was analyzed using X-rays photoelectron spectroscopy from Thermoscientific Nexa series. The surface area of as-prepared photocatalyst was recorded by nitrogen adsorption-desorption isotherm study using multipoint BET and BJH method at 77.4 K from Quantachrome Instrument. Mott-Schottky (MSK) and Electrochemical Impedance (EIS) measurements were carried out using metrohm potentiostat\galvanostat in 1 M Na_2SO_4 solution (as an electrolyte) at room temperature. The surface charge of the samples was analyzed using Zetasizer from Malvern series. The formation of free radicals was confirmed by using electron paramagnetic resonance (EPR) analysis from EMX micro–X Bruker series. Time correlated single photon counting (TCSPC) decay analysis was carried out using Edinburgh F980 instrument for monitoring the average recombination time of photogenerated species.

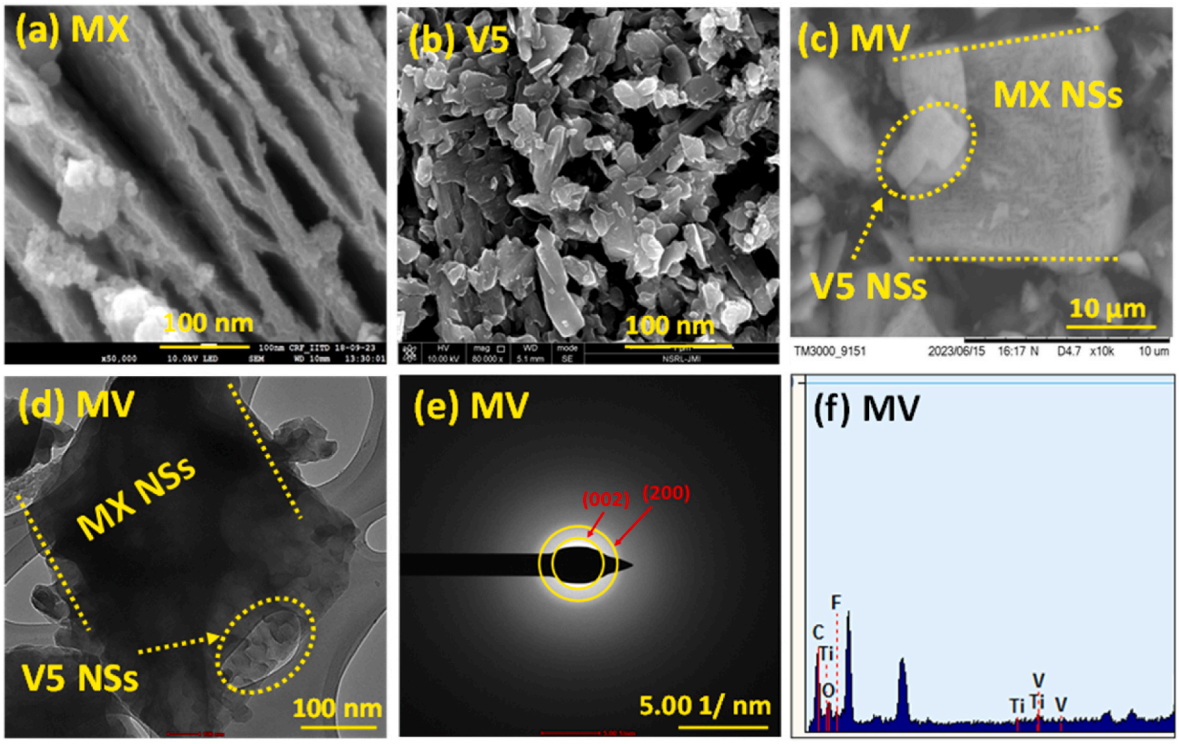

Fig. 2. FESEM image of (a) MX, (b) V5, (c) MV nanocomposite and HRTEM image of (d) MV, (e) SAED pattern of MV nanocomposite and (f) EDX spectrum of MV nanocomposite.

3. Results and discussions

3.1. Morphological analysis

Morphological study of the synthesized samples were performed using FESEM analysis as shown in Fig. 2(a–c). The stacked nanosheets of MXene having significant interlayer spacing are clearly visible in Fig. 2 (a) and also in good match with reported literature (Peng et al., 2022). The image of synthesized agglomerated nanosheets of V5 can be clearly observed in Fig. 2(b). The FESEM image of MV nanocomposite showing sheets of V5 are scattered on the surface of MX sheets as depicted in Fig. 2(c). The High-resolution TEM image of MV nanocomposite is shown in Fig. 2(d), nanosheets of MX as well as comparatively smaller nanosheets of pristine V5 both are clearly visible, confirming the existence of both the pristine morphologies in the nanocomposite. The larger sheets in nanocomposite corresponds to MX (dark in color) and smaller sheets correspond to V5 (bright in color), color contrast represents different atomic numbers. The SAED pattern of synthesized MV nanocomposite is depicted in Fig. 2(e), in which two different rings attributed for two planes (002) and (200) of MX and V5 samples having corresponding interplanar spacing of 1.48 nm and 0.653 nm, respectively. Fig. 2(f) depicts the EDX spectrum of the fabricated MV nanocomposite, indicating the presence of Titanium (Ti), Vanadium (V), Oxygen (O), Fluorine (F) and Carbon (C) in the MV nanocomposite. The absence of any other element in the as-synthesized MV nanocomposite demonstrates the purity of the synthesized sample.

3.2. XRD analysis

XRD analysis was carried out for detailed evaluation of crystallinity, crystal structure and associated orientation of synthesized samples. XRD diffractograms of the as-synthesized samples are given in Figs. S1(a–c). In XRD diffractogram of pristine MXene, as shown in Fig. S1(a), the peaks at 2θ values: 8.81°, 18.21°, 27.5°, 34.20°, 38.65°, 41.32°, 57.57° and 60.67° with interplanar spacing of 1.37 nm, 0.652 nm, 0.454 nm, 0.284 nm, 0.248 nm, 0.230 nm, 0.210 nm and 0.184 nm, respectively are attributed for the (hkl) planes: (002), (006), (008), (103), (104), (105), (109) and (110), respectively were in match with reported literature (Allen-Perry et al., 2021). In XRD diffractogram of pure V_2O_5 as shown in Fig. S1(b), the characteristic major peaks observed at 2θ values: 15.3°, 20.9°, 22.1°, 26.8°, 30.8°, 31.4°, 34.5° and 45.3° have been assigned to (hkl) planes: (200), (001), (110), (101), (301), (310) and (002), respectively. All the diffracted peaks are in match with reported literatures (Abd-Alghafour et al., 2016). The major diffracted peaks validates the presence of V_2O_5 in orthorhombic state. All the characteristic peaks of pristine samples are present in synthesized MV nanocomposite including 9.50°, 13.59°,17.78°, 18.71°,19.13°,22.9°, 24.67°, 25.57°, 28.50°, 31.78°, 35.9°, 38.98°, 41.83°, 48.36°, 56.74° and 60.26°, confirm the co-existence of both individual samples and represented with respective symbols as depicted in Fig. S1(c). In MV nanocomposite, the characteristic peak of MXene at 8.81° slightly shifts to higher angle at 9.5°. The minimal peak shift indicates that incorporation of V_2O_5 nanosheets did not significantly impact the interlayer distance of MXene as V_2O_5 nanosheets are dispersed over MXene sheets. The low intensity of V_2O_5 peaks in MV composite in XRD diffractogram might be due to complete dispersal of V_2O_5 nanosheets without aggregation of MXene. Also, V_2O_5 nanosheets have irregular and randomly oriented shapes scattered over MXene which also explains the low intensity of its peaks in composite. The composite material exhibits sharp diffraction peaks corresponding to both MXene and V_2O_5 which explains the crystalline nature of composite as also confirmed through SAED pattern. The extra peak at 25.57° in addition to peaks of V_2O_5 in MV may be an indication of presence of small TiO_2 which might be due to oxidation of MXene.

3.3. Fourier Transform Infrared (FTIR) analysis

The FTIR spectra of as-synthesized samples are shown in Figs. S1 (d–f)). The FTIR spectrum of MX is depicted in Fig. S1(d). The broad transmission bands observed at the 3325 cm^{-1} and 1120 cm^{-1} corresponds to stretching vibrations of hydroxyl group (-OH) and the presence of C–F bonds, respectively. The peak at 1630 cm^{-1} can be attributed to the presence of C═O bonds and the peak observed at 1335 cm^{-1} indicates the presence of water molecules (O–H) on the surface of MXene. The low intense peak observed at 620 cm^{-1} demonstrates the presence of Ti–O bond deformation vibration (Lee et al., 2017; Chen et al., 2019). In FTIR spectrum of V5 as depicted in Fig. S1(e), the intense transmission peaks observed at around 1015 cm^{-1} and 828 cm^{-1} are attributed to the stretching vibrations of V═O terminal bonds and the symmetric and asymmetric vibrations of V–*O*–V bonds, respectively. The low intensity peak observed at 538 $cm^{-1}$and 1730 cm^{-1} are due to the asymmetric stretching vibrations of triply coordinated oxygen atom and –OH bond, respectively. The low intense peak observed at 3420 cm^{-1} is attributed for bending vibration mode of H–*O*–H bond (Xavier, 2021). In FTIR spectra of synthesized MV nanocomposite as shown in Fig. S1(f), the presence of all the characteristic bands of individual materials shows better physiochemical interactions during the formation of nanocomposite.

3.4. Optical properties analysis

Optical properties of synthesized samples were studied using UV–visible absorption spectroscopy analysis. All the samples were dispersed in DI water through sonication for 20 min and the UV–Vis absorption spectrum was recorded. Then, the optical bandgap energy was evaluated by plotting Tauc's plot $((\alpha h\upsilon)^{1/n}$ vs $h\upsilon)$ as depicted in Figs. S2(a–c). Where h is the Planck's constant ($h = 6.626 \times 10^{-34}$ J s), ν is the frequency, α denotes the absorption coefficient having value of 2.303A/t, A represents the absorbance of the material and t represents the thickness of cuvette and n takes the value 2 for indirect band gap materials and the value ½ for direct band gap of materials. To calculate the energy band gap, the curve is linearly extrapolated from the first transition point and the intercept on x-axis gives the value of bandgap energy. The bandgap energies observed for the pure MXene, V5 and MV nanocomposite are 1.58 eV, 2.70 eV and 2.15 eV, respectively. It can be concluded from the graph, that the value of energy bandgap of the MV nanocomposite lies in between that of the corresponding pure components. The red shift in the bandgap energy observed from pure V_2O_5 to the nanocomposite can be attributed for the contribution of the highly conducting property of MXene, which enhances light absorption in both UV and visible region for the nanocomposite, resulting in a better photocatalyst and a promising candidate for wastewater pollutant degradation (Tahir et al., 2022). The value of bandgap in nanocomposite provides an enhanced electron mobility and potentially improved light absorption capabilities makes composite more suitable for the removal of pollutants from wastewater.

3.5. X-rays photoelectron spectroscopy (XPS) analysis

X-ray photoelectron spectroscopy was carried out for analyzing the elemental composition and surface properties of synthesized MV nanocomposite, as it is constituent of two distinct phases, but exhibits the promising properties of both the individual entities. Fig. 3(a–f), depicts in-depth XPS characterization of MV nanocomposite with its all-constituents elements. The interactions of chemical bonding and any other synergistic effect, arising from the combination of individual materials $Ti_3C_2T_x$ (MX) and V_2O_5 (V5) on their interface is also analyzed. Fig. 3(a) shows the core level XPS scan of MV nanocomposite in the range of 0–800 eV, and indicates that constituent elements are Ti, V, C, O and F. In the XPS spectrum of Ti 2p as shown in Fig. 3(b), peaks are deconvoluted into the majority of two groups: one is, Ti atoms linked

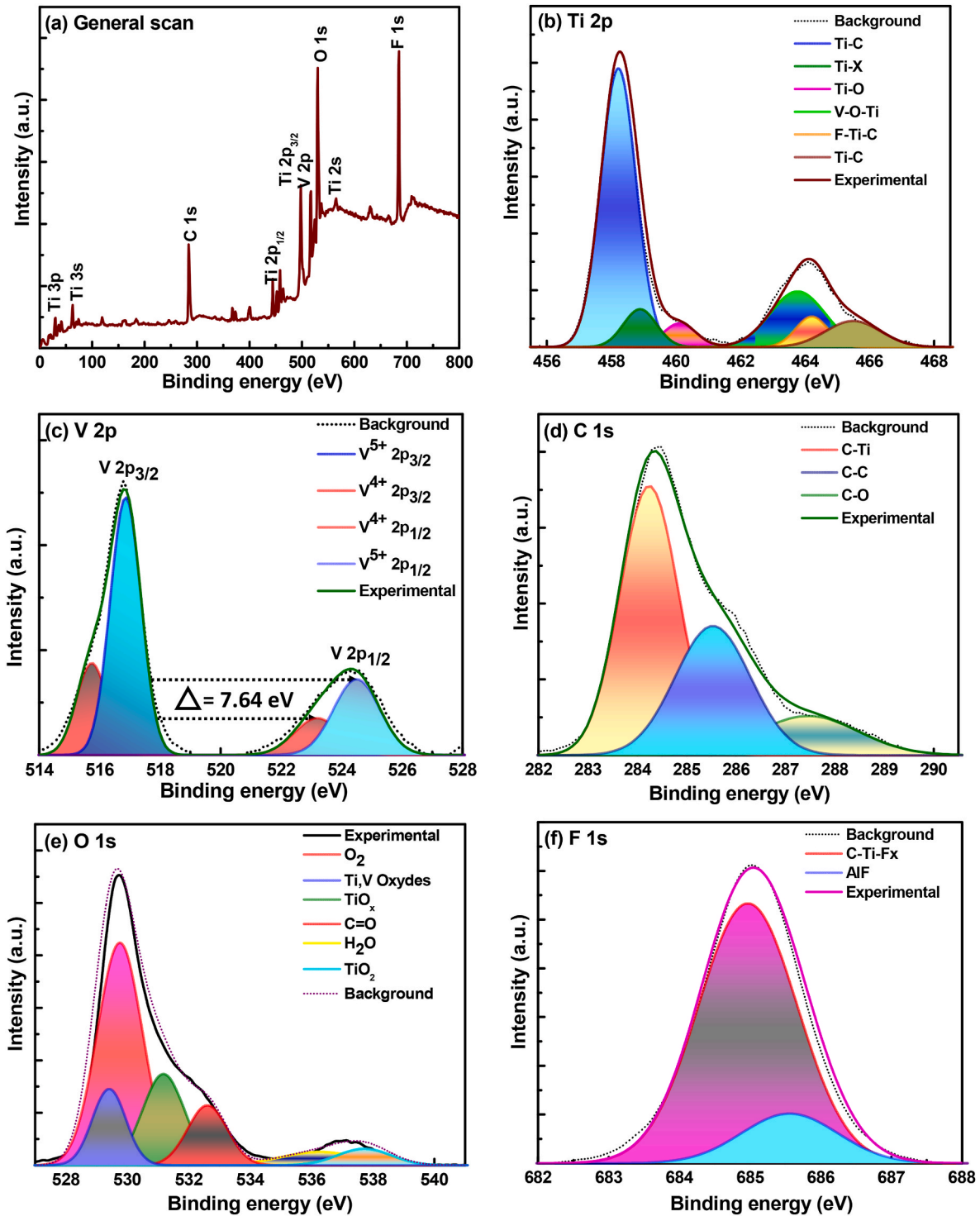

Fig. 3. (a) General level XPS scan, and core level scans of (b) Ti 2p, (c) V 2p, (d) C 1s, (e) O 1s and (f) F 1s of MV nanocomposite.

to the O groups such as (V–*O*–Ti and Ti–O) and another is in which Ti atom is linked with the termination groups such as (Ti–C and F–Ti–C), which may be the results of surface oxidation. In XPS spectrum of V 2p as shown in Fig. 3(c), The peak at 524.3 eV is assigned to V $2p_{1/2}$ and deconvoluted to V^{+4} and V^{+5} oxidation states of vanadium having binding energies at 523.3 eV and 524.5 eV respectively. The peak at 516.8 eV is assigned to V $2p_{3/2}$ and deconvoluted to V^{+4} and V^{+5} oxidation states of vanadium at binding energies at 515.74 eV and 516.86 eV, respectively. The binding energy difference between spin states for V^{+4} oxidation state is 7.64 eV. The binding energy difference between spin states 3/2 and 1/2 for V^{+5} oxidation state is 7.64 eV. The area ratio depicting intensities are in ratio 2:1 for spin states 3/2 and 1/2 for both V^{+4} and V^{+5} oxidation states. The full width at half maxima (FWHM) for spin state 3/2 for both V^{+4} and V^{+5} oxidation states is 1.2 and for spin state 1/2 for both V^{+4} and V^{+5} oxidation states is 1.8 (Akande et al., 2018).

In core level XPS spectrum of C1s as depicted in Fig. 3(d), three components at 284.2, 285.5 and 287.4 eV attributed for Ti–C bonds of MXene phase with Ti_3C_2, C–C bond and C–O bonds, respectively. In XPS scan of O 1s as represented in Fig. 3(e), the peaks at 529.2, 529.7, 531.2,

532.6, 536.2 and 537.6 eV attributed for Ti, V oxydes, O_2, TiO_x, C═O, H_2O and TiO_2, respectively (Wang et al., 2019). In F 1s core level spectrum as shown in Fig. 3(f), peak at 684.9 eV can be attributed for Ti–F surface termination and another peak at 685.6 eV indicates AlF contamination as a consequence of etching of Ti_3C_2 from Ti_3AlC_2 using fluoride-based etchant (Lim et al., 2021). On the basis of XRD and XPS studies, it is concluded that MV nanocomposite has been synthesized successfully, and small shifts in binding energy from their pristine individuals confirm the formation of new chemical species at MV interface and occurrence of synergistic effects, which plays crucial role in the removal of contamination from wastewater.

3.6. Mott-Schottky analysis

For analyzing the band-edge positions, semiconducting nature, and carrier concentration of the synthesized samples Mott-Schottky (MSK) experiment was performed by depositing the sample on working electrode in 1 M Na_2SO_4 solution as an electrolyte. In the MSK plots of MX, V5 and MV as shown in Figs. S3(a–c), the positive character of slopes demonstrate n-type behavior with values of flat band potentials −0.94, −0.48 and −0.29 V, respectively. In general, for n-type nature of semiconductor flat band potential is close to conduction band potentials and values of band edge positions (valence band, conduction band) are calculated using equations (1) and (2).

$$V_{CB} = V_{F\ NHE,pH=7} = V_{F\ Ag/AgCl} - 0.059(7 - pH\ of\ elecrolyte\ used) + 0.198 \quad (1)$$

$$V_{VB} = V_{CB} + \frac{E_g}{e} \quad (2)$$

Where, V_{CB} and V_{VB} are the potential values of conduction band and valence band, respectively. The carrier densities of the synthesized materials are calculated using equation (3), and the obtained values are listed in Table 1.

$$N_d = \frac{2}{e\varepsilon\varepsilon_o}\left[\frac{d\left(\frac{1}{C^2}\right)}{dV}\right]^{-1} \quad (3)$$

Where, N_d represents the density of charge carrier, $\frac{d\left(\frac{1}{C^2}\right)}{dV}$ is the slope from MSK curve, $e, \varepsilon\ and\ \varepsilon_o$ are the charge of the electron, dielectric constant of materials, and permittivity in vacuum, respectively. The values of ε for pure MXene and V_2O_5 are 60 and 9, respectively.

The values of flat band potential as obtained from Mott Schottky plots, calculated carrier concentration for MV sample is much higher (6.3 X 10^{32} cm^{-3}) as compared to both the pristine samples, which provides an ease of movement of charge carriers and helps in the breakdown of CV molecules into the simpler or non-toxic products. The higher carrier concentration of synthesized MV nanocomposite as compared to pristine MX and V5 thus makes it better material for the photocatalytic degradation of pollutants and other applications.

Table 1
Band-edge positions, bandgap (E_g) and carrier concentrations (N_d) calculated from MSK curves for MX, V5 and MV samples.

Samples	Flat band potential (V_F)	V_{CB} (V)	V_{VB} (V)	Bandgap E_g (eV)	N_d (cm^{-3})
MX	−0.94	−0.77	0.81	1.58	2.0×10^{30}
V5	−0.48	−0.31	2.39	2.70	1.5×10^{31}
MV	−0.29	−0.12	2.03	2.15	6.3×10^{32}

4. Photocatalytic parameters

Crystal Violet (CV) a textile dye, was used to study the photocatalytic activity of the synthesized MV nanocomposite, along with the pristine samples MX and V5. The degradation study of the prepared samples against CV dye was carried out in dark for adsorption-desorption equilibrium for a period of 60 min, followed by photo-degradation observations for equal period of 60 min in the irradiation of light. The study was conducted with respect to variable concentrations of dye (10, 20 and 30 ppm) in deionized (DI) water, to evaluate the effect of initial concentration of pollutants on the efficiency of the synthesized samples. For performing the experiment, 20 mg of each sample (MX, V5 and MV) was added to separate beakers containing 10 ppm of CV dye solution for a comparative study of removal efficiency. Each solution was initially stirred in dark conditions and at intermediate time intervals the stirring was turned off to collect samples. Approximately, 2 mL of sample was collected and centrifuged to separate the catalyst particles and the remaining degraded solution was exposed to UV–Vis spectroscopy to analyze the absorption peaks and removal efficiency for CV. Then, same process was repeated in the presence of light for the same interval of time. Under similar conditions the experiment was repeated for 20 and 30 ppm concentrations of CV dye.

4.1. Photocatalytic activity and rate kinetic analysis

The absorption spectrum for CV removal using various samples at different dye concentrations is shown in Figs. S4(a–i), and it can be concluded that the degradation activity of MV was maximum at all the concentrations, whereas the pristine MX showed the least degradation efficiencies. Maximum degradation efficiency by MV was achieved within initial 10 min, with corresponding efficiencies of ~60 %, ~50 % and ~40 % under dark conditions. The synthesized MV sample degrades more than 50 % of CV under dark conditions hence, proves much better catalyst than other reported samples as summarized in Table S1.

Photocatalytic efficiency (η %) was evaluated using equation (4) as given below:

$$\eta = \left(1 - \frac{C_t}{C_0}\right) \times 100\ \% \quad (4)$$

The graphical representation of degradation efficiency with respect to time at different dye concentration is shown in Figs. S4(j–l),

To analyze the adsorption mechanism during the photocatalytic study both Pseudo first and second order rate kinetics studies were carried out. Pseudo first order rate kinetics deal with the process of physisorption, where the only substantial interaction is the weak Vander Waal's interaction, with the absence of any chemical reactions between the particles of adsorbate and adsorbent.

First order rate kinetics is governed by equations (5) and (6) as given below.

$$C_t = C_0 e^{-K_1 t} \quad (5)$$

$$-ln\ \frac{C_t}{C_0} = K_1 t \quad (6)$$

Where, K_1 is the rate constant corresponding to the kinetics, C_t and C_0 are the intensities of absorption at time t and at initial time, respectively. Thus, the first order rate constants are given by the slope of the graph plotted between $-ln\ \frac{C_t}{C_0}$ and t. The value of correlation coefficients (R^2) approximately equal to 1, suggests that the reaction follows particular order rate kinetics.

Pseudo second order kinetics governs the process which involves chemisorption's, i.e., the process in which formation of bonds are involved. Equations governing the second order rate kinetics are given below equation (7).

$$Q_t = \frac{1}{K_2 Q_e^{\,2}} + \frac{1}{Q_e} \tag{7}$$

Where, K_2 is the rate constant corresponding to the second order kinetics, Q_t and Q_e are the amount of adsorbed dye at time t and at the time at which system achieves equilibrium, respectively.

The plots of ratio of absorption concentrations at specific time 't' (C_t) and initially (C_0) and other rate kinetic plots are given in Fig. 4(a–f) for better understanding of the rate kinetics and degradation efficiency.

The maximum efficiency of each sample at different dye concentration was observed over a period of 120 min, followed by 60 min of adsorption in dark and 60 min of photo-degradation in light irradiation. The fitting of rate kinetics graphs is only done under light conditions and all the parameters for rate kinetic studies are summarized in Table 2. As it is clear from Fig. 4(a–f) and Table 2, that there is an inverse relation between the initial concentration of the pollutant and the degradation efficiency observed, for constant photo-catalyst quantity. The obtained values of correlation coefficient R_1^2 from the graphs, suggests that in case of MX, V5 and MV nanocomposite pseudo first order rate kinetic mechanism was followed, suggesting that physisorption is the main factor for the removal of CV molecules. The values of rate constants (K_1) reveal the fastness of the process and from the obtained values it can be

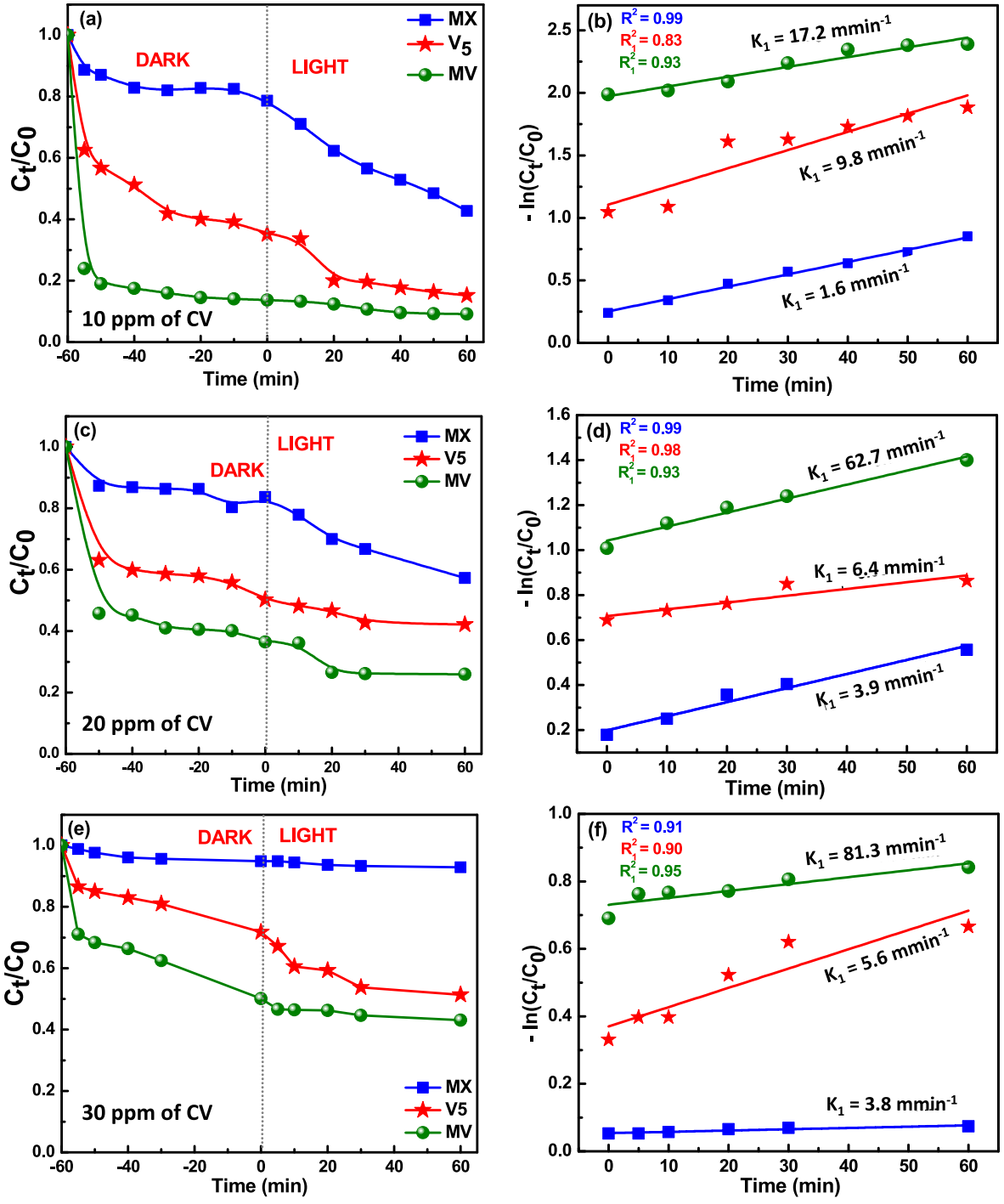

Fig. 4. Pseudo-first order rate kinetics C_t/C_0 and $-\ln C_t/C_0$ plots for MX, V5 and MV nanocomposite at (a–b) 10 ppm, (c–d) 20 ppm and (e–f) 30 ppm, concentrations of CV, respectively.

Table 2
The efficiency and rate kinetics parameters of MX, V5 and MV for the removal of CV dye.

Samples	Pollutant (CV) concentrations		
	10 ppm		
Samples/Parameters	**η %**	R_1^2	K_1 ($mmin^{-1}$)
MV	92.8 %	0.93	17.2
MX	57.3 %	0.99	1.6
V5	81.2 %	0.83	9.8
20 ppm			
Samples/Parameters	**η %**	R_1^2	K_1($mmin^{-1}$)
MV	76.5 %	0.93	62.7
MX	41.3 %	0.99	3.9
V5	59.2 %	0.98	6.4
30 ppm			
Samples/Parameters	**η %**	R_1^2	K_1($mmin^{-1}$)
MV	58.6 %	0.85	81.3
MX	7.1 %	0.91	3.8
V5	45.3 %	0.90	5.6

concluded that during photocatalytic process, removal rate for MV nanocomposite is ~2, 10 and 15 folds faster than pristine MX for 10, 20 and 30 ppm concentration of CV dye.

4.2. Mechanism for photocatalytic degradation

For understanding the mechanism of augmentation of the degradation of CV using MV nanocomposite, the separation of charges at the interface of pristine materials was investigated and possible S-scheme degradation mechanism is as shown in Scheme 1. According to S-scheme mechanism two n-type semiconductors one having high energy of conduction band called reduction photocatalyst (RP) and other having low conduction band energy called oxidation photocatalyst (OP). Here, MX acts as RP and V5 works as OP and the band edge positions V_{CB} and V_{VB} of MX (−0.77 and 0.81 eV), and V5 are (−0.31 and 2.39 eV). The obtained V_{CB} value for MX is −0.77 eV is superior than the redox potential of O_2/O_2^- (−0.33 eV), hence reduction takes place from the surface of MX. Similarly, the oxidation of H_2O to form OH^- might be possible from the valence band (VB) of V5 due to the sufficient energy (2.39 eV) for this conversion. Consequently, the migration of charge carriers in this case will follow typical S-scheme heterojunction mechanism (Kane et al., 2022; Xue et al., 2022). Electrons in the synthesized MV nanocomposite migrate from the valence band (VB) to the conduction band (CB) when exposed to an appropriate amount of radiation that exceeds the band gap energy, leaving holes behind. These electrons move from the CB of V5 to VB of MX for the recombination. Then, the left-out electron in CB of MX and holes in VB of V5 will further participate in the photocatalytic reaction and plays vital role in the degradation of CV dye. Previously reported works also show that MX works as a good electron capturing mediator during the photocatalytic process and surface functionalization of MX as explained in FTIR section also improve electrons mobility results in the complete mineralization of pollutants into water and carbon dioxide molecules (Hu et al., 2021). Expected reactions during the mineralization of CV during photocatalytic reaction in water are given in equations (8)–(11) (Kaur et al., 2024; Hu et al., 2022).

$$MV\ (Catalyst) \rightarrow e^- + h^+ \quad (8)$$

$$e^- + O_2 \rightarrow O_2^- \quad (9)$$

$$OH^- + h^+ \rightarrow OH^{\cdot} \quad (10)$$

$$CV + OH^{\cdot} \,/\, O_2^- \rightarrow Degraded\ products + H_2O + CO_2 \quad (11)$$

4.3. Electrochemical Impedance spectroscopy (EIS) analysis

To investigate the kinetics of ions transportation at the interface EIS technique was studied and Nyquist plots were analyzed in 1 M Na_2SO_4 solution as an electrolyte as shown in Fig. S5(a). The x-intercept of the plots gives the value of solution resistance (R_s) and the diameter of the semicircular arc provides the value of charge transfer resistance (R_{ct}). Pristine MX and V5 both have the largest diameter of semicircular arc demonstrating value of R_{ct} 5.6 and 3.1 Ω, respectively which hinders in the movement of charge carries. As depicted in Fig. S5(a), the lowest diameter of the semicircle in case of MV nanocomposite results in more active sites and good charge transport nature as compared to pristine samples. The smallest value of R_{ct} 1.3 Ω for MV nanocomposite makes it better material for the catalytic activity and for the energy storage devices and the obtained photocatalytic degradation results of CV are also in good agreement with this data.

4.4. Effect of temperature and catalyst dosage

The effect of temperature on the removal efficiency of CV was studied at 30 ppm concentration of dye for 60 min under dark conditions and obtained results are shown in Fig. 5(a). An increase in the solution temperature from 40, 60 and 80 °C increases the removal efficiency of CV 83, 94 and 99 %, respectively with an error of ±2 % in 60 min. The increase in the efficiency can be attributed that rising in the temperature greatly promotes the diffusion and collision of reactive radicals and ions in the solution and consequently results in the enhanced removal efficiency.

Fig. 5(b), illustrates the effect of dosages of MV nanocomposite on the removal efficiency of dye. For carrying out this study, 30 ppm of dye concentration for 60 min under dark conditions was used to analyze the effect of MV dosage (0.2, 0.4, 0.6, 0.8 and 1.0 mg/L) on the removal efficiency. The removal efficiency tends to increase on increasing the dosage of MV catalyst, efficiency increased from 58 % to 98 ± 2 % on increasing the catalyst dosage from 0.2 to 1 mg/L. The greater surface area and the larger number of accessible adsorption sites may be responsible for the enhanced removal efficiency of CV.

4.5. Surface charge analysis and pH dependent study

The surface charge of all the synthesized samples was studied via zeta potential measurement as shown in Fig. S5(b). The surface charge corresponding to the photo-catalyst is an important factor during the photocatalytic dye degradation process. For a dispersed particle, its surface develops an electric charge due to the interaction with its surroundings, leading to formation of two separate regions around the particle, the inner region called the stern layer and the outer region termed as the diffuse layer (Wang et al., 2022). The zeta potential represents the potential difference between these two regions. Surface potential associated with MX, V5 and MV was found to be −12.5 mV, −33.7 mV and −27.8 mV respectively, implying that negative surface charge resides for all the samples and the degradation against a cationic dye is expected to be much more owing to competitive adsorption. The high value of surface charge in case of MV nanocomposite as compared to pristine MX, makes the sample more stable for the catalytic application. The observed results from photocatalytic studies can be well inferred from zeta potential analysis. The values of zeta potential study are summarized in Table S1. The zeta potential also carried out with auto-titration at different pH ranging from 1 to 12, which shows that the MV sample does not have any isoelectric point or point of zero charge (PZC), beyond which the surface of MV sample become positive and at all pH values surface charge is negative. These results are compatible with those of photocatalytic results, since the sample is not suited for the removal of anionic dyes, because of repulsive electrostatic interactions between the anionic dyes' surface and the negative surface charge of MV

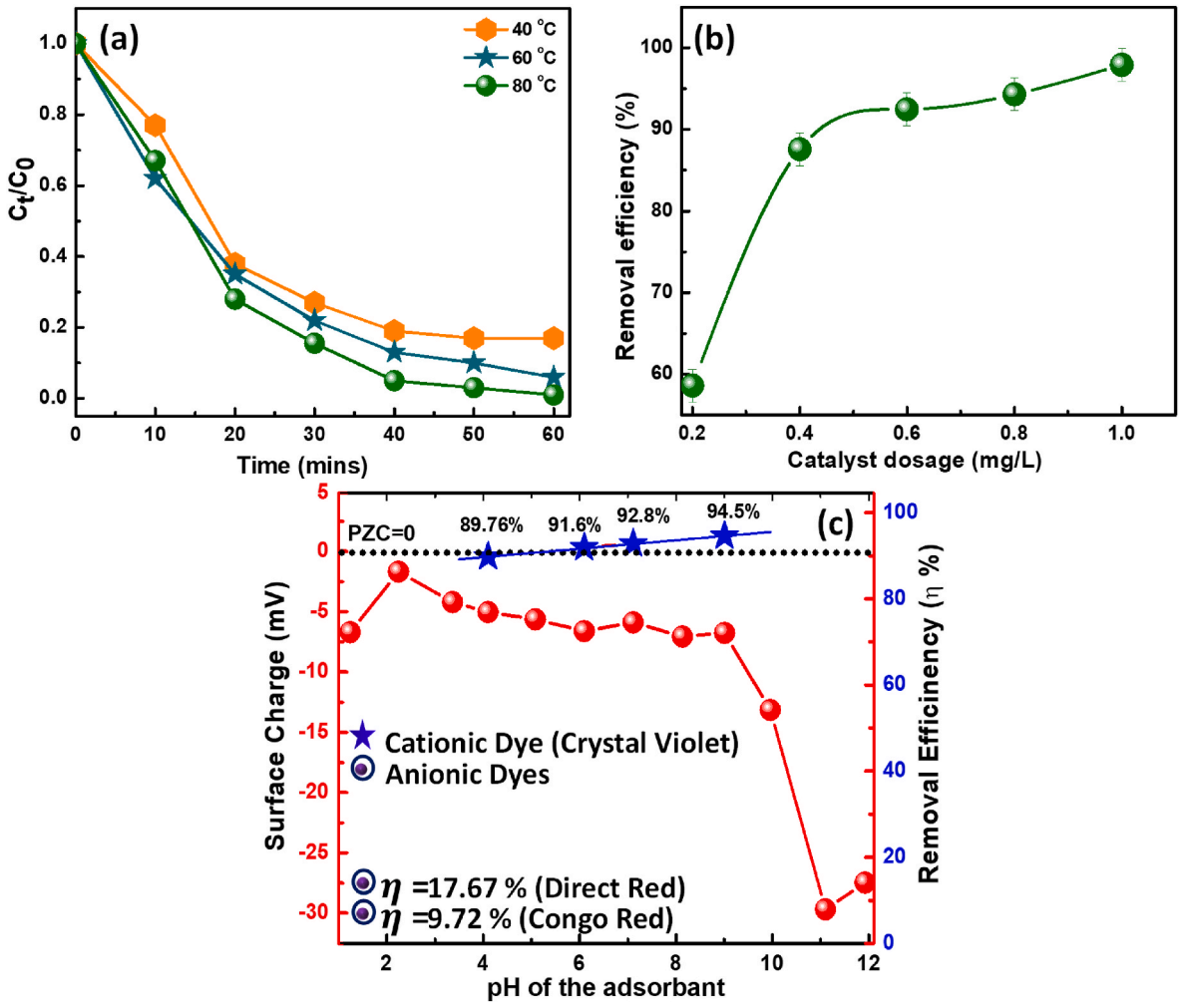

Fig. 5. Effect of (a) temperature at 40, 60 and 80 °C, (b) catalyst dosage on the removal efficiency of CV and (c) solution pH on the adsorption efficiency and point of zero charge for MV nanocomposite (dotted circles shows efficiency for DR and CR at 7.1 natural pH of sample).

sample. The removal efficiency for anionic dyes direct red (DR) and congo red (CR) found out to be 9.72 and 17.67%, respectively. The MV composite only shows negative surface charge through out the entire range of pH (1–12) without attaining isoelectric point or point of zero charge (PZC). Hence, it can be easily concluded that the sample is only suitable for the removal of cationic dyes only due to good electrostatic interaction. The removal efficiency at different pH and surface charge variation with pH is shown in Fig. 5(c).

4.6. Time-Correlated Single Photon Counting decay

The average lifetime of the photogenerated charge carriers and dynamics was evaluated by Time-Correlated Single Photon Counting (TCSPC) decay as shown in Fig. S5(c). The decay curves of the synthesized samples were simulated using a triexponential model using the following equation (12).

$$y = A + B_1 e^{-i/T_1} + B_2 e^{-i/T_2} + B_3 e^{-i/T_3} \quad (12)$$

Where, B_1, B_2 and B_3 represent the amplitude of the components corresponding to 1, 2 and 3, respectively. T_1, T_2 and T_3 belong to the average lifetime corresponding to the slow, intermediate, and fast decays. The obtained value of $\chi 2$ (~1), shows the best fit for the experimental data. The recombination through inter-band exciton process results in fast photoluminescence (PL) decay, whereas recombination of photogenerated species in an indirect mode leads for the slow PL decay. The average lifetime (T_{av}) was calculated using equation (13).

$$T_{av} = \frac{B_1 T_1^2 + B_2 T_2^2 + B_3 T_3^2}{B_1 T_1 + B_2 T_2 + B_3 T_3} \quad (13)$$

For pure MX and V5 the average lifetime T_{av} was found to be 3.97 ns and 1.75 ns, respectively. For synthesized MV nanocomposite, T_{av} is 5.20 ns which is much higher than pristine samples. The results of TCSPC decay fitting for pristine MX, V5 and MV nanocomposite are tabulated in Table S2. The average lifetime for MV nanocomposite was found to be much higher than the pristine samples, makes it better for the removal of pollutants from wastewater and in correlation with the obtained photocatalytic results for the degradation of CV dye.

4.7. Surface area analysis

The analysis of specific surface area (S.S.A.) and pore diameter of as-synthesized MV nanocomposite was carried out through BET characterization technique. The nitrogen adsorption and desorption isotherms evaluation were performed at temperature 77.5 K and displayed as the plot of volume absorbed with respect to the relative pressure (P/P_o), as shown in Fig. 6(a). The plot indicates the consistency with isotherms of type IV, demonstrating mesoporous nature of the synthesized nanocomposite. Graphical representation for pore size investigation was done through BJH technique, as depicted in Fig. 6(b). The value obtained of the specific surface area specified according to the BET multipoint method and the BJH method is 9.57 m^2/g and 13.11 m^2/g,

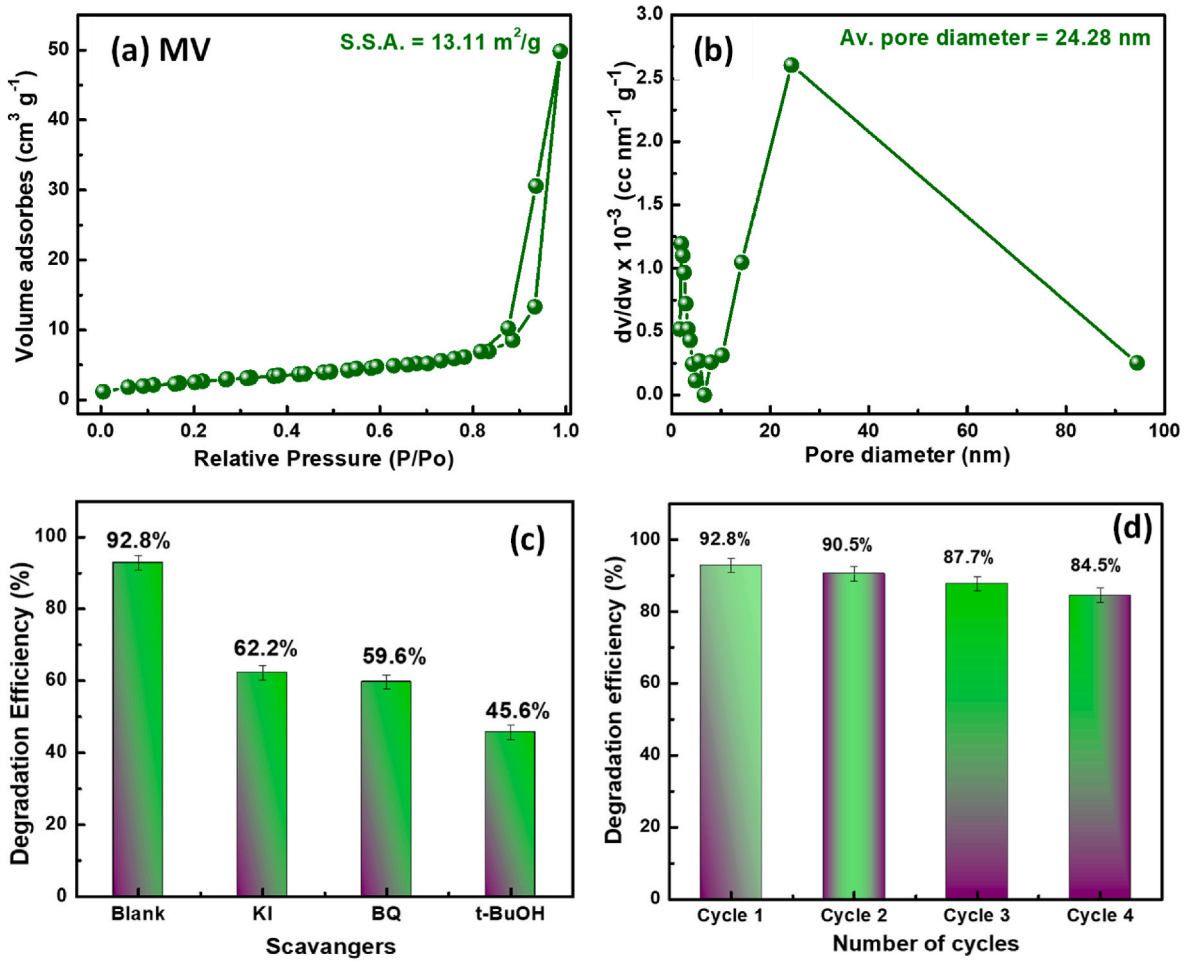

Fig. 6. (a) BET isotherms, (b) BJH plots for the synthesized MV nanocomposite, (c) Trapping and (d) reusability study using MV nanocomposite against CV dye.

respectively and the average pore diameter value of pore diameter for the synthesized MV nanocomposite is 24.28 nm. The resulting higher values of MV nanocomposite from the pristine samples Ti_3C_2 MXene (4.74 m^2/g) and V_2O_5 (4.5 m^2/g), makes it better material with enhanced catalytic properties (Bordoni et al., 1994; Tawalbeh et al., 2023). The charge transport is assisted via the mesoporous conductive network providing better photocatalytic property also in match with the photocatalytic degradation results.

4.8. Chemical oxygen demand (COD) analysis

The chemical oxygen demand (COD) test is used to analyze the organic strength and toxicity of polluted and treated water. The measurement for the total quantity of oxygen required to oxidize the organic matters in form of water and CO_2 was carried out using COD analysis. The COD value of CV dye solution and after treatment using MV nanocomposite was found to be 174 and 32 ppm, respectively. The reduction in COD value shows the complete mineralization of wastewater into non-toxic products along the decolorization.

Equation (14) was used to quantify degradation as a percentage reduction of COD (Zhang et al., 2021).

$$\%\ COD_{reduction} = \frac{COD_{initial} - COD_{final}}{COD_{initial}}\ X\ 100 \tag{14}$$

Where, $COD_{initial}$ is the COD value of untreated water and COD_{final} is the COD value of treated water using MV nanocomposite.

The % reduction in COD value was 81.60%, obtained using above equation. The obtained results demonstrate the reduction in toxicity for the treated sample to a great extent.

4.9. Trapping study and reusability test

To have a better perception towards the degradation process followed, it is inherent to understand the role of active species generated in presence of photons. In order to investigate these factors, experiments with a set of scavengers were performed, specifically tetra butanol (t-BuOH) was used capturing for $OH^{\cdot}$, 1–4 benzoquinone (BQ) entraps $O_2^{\cdot-}$, whereas potassium iodide (KI) traps both h^+ and $OH^{\cdot}$. The presence of these scavengers inhibits the action of the specified reactive species, resulting in the decrease of the degradation efficiency associated with the photocatalyst alone. The resultant efficiencies observed during the photocatalyst study for MV using scavengers are summarized in Fig. 6 (c). It is concluded that the maximum deficiency in photocatalytic study was observed for the case of t-BuOH, indicating $OH^{\cdot}$ being the primary species in the degradation of CV using MV nanocomposite. The presence of KI affected the efficiency of the degradation process least as compared to other scavengers, that h^+ being the least affecting parameters in the photodegradation mechanism. The efficiency of BQ was found to have significant deficiency, suggesting that $O_2^{\cdot-}$ are the secondary species during the process. Overall, a significant decrease in the efficiency was observed for all the scavengers, implying that every reactive species played a significant role in the degradation process observed of textile dye.

For increased sustainability, it is desired that the photocatalyst should be reproducible and reusable for number of cycles. The reusability of the synthesized nanocomposite was studied by analyzing the

removal efficiency in consecutively four cycles. The experiment was conducted using 20 mg of MV nanocomposite for the removal of 10 ppm concentrated crystal violet dye. Approximately 2 mL of the degraded solution was collected at equal intermediate time intervals, and its absorbance was recorded. Then the photocatalyst was separated from the dye solution through centrifugation, followed by washing with DI water using vacuum filtration method and drying at 60 °C. Afterward, the obtained MV photocatalyst reused again with the addition of equally concentrated dye solution for next cycles. The same procedure was carried out four times and the obtained results for photocatalytic efficiency are shown in Fig. 6(d). Thus, it can be concluded that on an average only ~2% decrease in the efficiency was observed for each consecutive cycle, emphasizing the potential of the photocatalyst to be effectively used for five or more times.

4.10. EPR analysis

Electron paramagnetic resonance (EPR) analysis was carried out to monitor the formation of hydroxyl $OH^{\cdot}$ and superoxide O_2^{-} radicals. The aqueous solution of DMPO was used to capture $OH^{\cdot}$ and methanol solution to catch O_2^{-}. As results are shown in Fig. 7(a & b), both DMPO-$OH^{\cdot}$ and DMPO-O_2^{-} adducts shows intermediate and strong characteristic signals under dark and light conditions, respectively. The intermediate signals under dark conditions support photocatalytic results that more than 60% degradation of CV takes place and strong signals demonstrates that under light irradiation generation of radicals enhanced significantly, results in the complete degradation of CV dye. Higher intensity of $OH^{\cdot}$ radicals and more drift velocity than O_2^{-}, predicts that $OH^{\cdot}$ are the primary and O_2^{-} are secondary species in degradation process and also in support of the trapping study.

The values of lande g-factor are calculated by using equation (15) as given below;

$$g = h\upsilon/\mu_B H \tag{15}$$

Where, h (6.62×10^{-34}Js) is Planck's constant, υ (9.48 GHz) is the frequency of X band, μ_B (9.27×10^{-21}J/T) represents Bohr magneton and H is the value of the magnetic field at origin. The values of g comes out to be 2.03 and 2.04 for $OH^{\cdot}$ radicals under dark and light illuminations as represented in Fig. 7(c & d). For O_2^{-} radicals, values of g are 2.02 and 2.03 under dark and light conditions. These values of g-factor provide good shred of evidence for the formation of free radicals during photocatalytic process and in complete agreement with the results of catalytic and scavenger studies.

5. Conclusion

This research work has focused on the successfully and efficiently synthesis of MXene and V_2O_5 (MV) nanocomposite via hydrothermal method. The addition of V_2O_5 in the pristine MXene ($Ti_3C_2T_x$) helps in significantly enhancing the photocatalytic degradation efficiency of CV dye via S-scheme based photocatalytic mechanism. The incorporation of

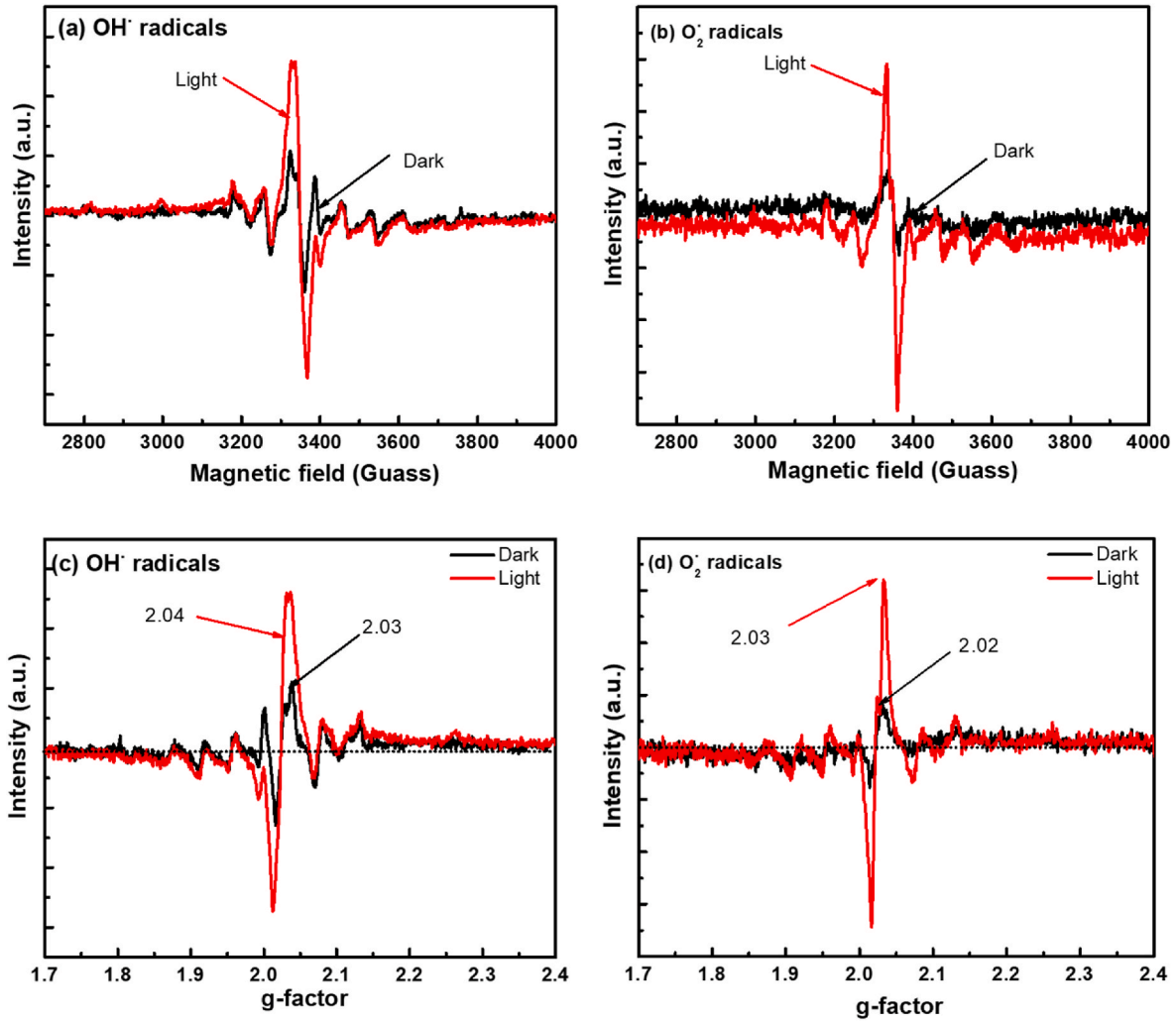

Fig. 7. EPR and lande g-factor plots for (a,c) $OH^{\cdot}$ radicals (b,d) O_2^{-} radicals, under dark and light conditions.

V_2O_5 in MXene sheets helps in improving the surface area (as analyzed from BET), optimization of surface charge (as investigated from zeta potential) and enhancing the movement of charge carriers (as analyzed from EIS study), resulting in the enhancement of removal efficiency. The synthesized MV nanocomposite has attained removal efficiency up to 92 %, 76 % and 58 % with an error of ±2 % at 10, 20 and 30 ppm concentration of CV from wastewater. The degradation mechanism was analyzed and followed S-scheme mechanism helps in reducing the recombination rate of photogenerated species. In order to get insightful impact on the active species in degradation mechanism trapping experiment was also performed and concluded that O_2^- and OH· are the primary and secondary active radicals which were further confirmed using electron paramagnetic resonance analysis. The COD test explains about the organic strength and toxicity of polluted and treated water. The enhanced understanding of the composition of surface of materials and optimization for various specific applications: including catalysis, energy storage, and electronic devices can be made possible with XPS analysis. Synthesized sample are also stable, non-toxic, and reusable hence can be regenerated and reused many times, helps in reducing the cost at industrial level. The synthesized nanocomposite in this work could have potential applications in the use of adsorption and the photocatalytic degradation of organic pollutants from wastewater, water splitting and so on.

CRediT authorship contribution statement

Nahid Tyagi: Writing – review & editing, Writing – original draft, Visualization, Software, Methodology, Investigation, Data curation, Conceptualization. **Diksha Sharma:** Writing – original draft, Software, Methodology, Formal analysis. **Manika Khanuja:** Visualization, Supervision, Resources, Project administration, Funding acquisition, Formal analysis.

Funding

Support of Department of science and Technology, India [DST/NM/NB/2018/203(G)(JMI)] and University Grants Commission [F. 4-5(201-FRP)/2015(BSR)] is highly acknowledged. Nanoscale Research Facility (NRF) under the project INUP-i2i (RP04176) funded by MeitY, IIT Delhi is also acknowledged for providing characterization facilities to compile this research work.

Declaration of competing interest

The authors declare that they have no known competing financial interests or personal relationships that could have appeared to influence the work reported in this article.

Appendix A. Supplementary data

Supplementary data to this article can be found online at https://doi.org/10.1016/j.chemosphere.2024.143971.

Data availability

The authors do not have permission to share data.

References

Abd-Alghafour, N., Ahmed, N.M., Hassan, Z., 2016. Fabrication and characterization of V_2O_5 nanorods based metal–semiconductor–metal photodetector. Sensor Actuator Phys. 250, 250–257.

Akande, A.A., Machatine, A.G.J., Masina, B., Chimowa, G., Matsoso, B., Roro, K., Duvenhage, M.-M., Swart, H., Bandyopadhyay, J., Ray, S.S., Mwakikunga, B.W., 2018. Blue- and red-shifts of V_2O_5 phonons in NH_3 environment by in situ Raman spectroscopy. J. Phys. Appl. Phys. 51, 015106.

Allen-Perry, K., Straka, W., Keith, D., Han, S., Reynolds, L., Gautam, B., Autrey, D.E., 2021. Tuning the magnetic properties of two-dimensional MXenes by chemical etching. Materials 14, 694.

Allen, N.S., Edge, M., Verran, J., Stratton, J., Maltby, J., Bygott, C., 2008. Photocatalytic titania based surfaces: environmental benefits. Polym. Degrad. Stabil. 93, 1632–1646.

Ashraf, W., Khan, A., Bansal, S., Khanuja, M., 2022. Mechanical ball milling: a sustainable route to induce structural transformations in tungsten disulfide for its photocatalytic applications. Phys. E Low-dimens. Syst. Nanostruct. 140, 115152.

Bansal, S., Singh, A., Poddar, D., Jain, P., 2023. Fabrication and photocatalytic evaluation of functionalized chitosan decorated vanadium pentoxide nano-adsorbents for water remediation. Ceram. Int. 49, 8871–8885.

Baynosa, M.L., Mady, A.H., Kumar, D.R., Sayed, M.S., Tuma, D., Shim, J.-J., 2020. Eco-friendly synthesis of recyclable mesoporous zinc ferrite@reduced graphene oxide nanocomposite for efficient photocatalytic dye degradation under solar radiation. J. Colloid Interface Sci. 561, 459–469.

Bojarczuk, A., Jelonkiewicz, Ł., Lenart-Boroń, A., 2018. The effect of anthropogenic and natural factors on the prevalence of physicochemical parameters of water and bacterial water quality indicators along the river Białka, southern Poland. Environ. Sci. Pollut. Control Ser. 25, 10102–10114.

Bordoni, S., Castellani, F., Cavani, F., Trifiro, F., Gazzano, M., 1994. Nature of vanadium species in SnO_2- V_2O_5-based catalysts. Chemistry of preparation, characterization, thermal stability and reactivity in ethane oxidative dehydrogenation over V–Sn mixed oxides. J. Chem. Soc., Faraday Trans. 90, 2981–3000.

Cai, H., Wang, B., Xiong, L., Bi, J., Yuan, L., Yang, G., Yang, S., 2019. Orienting the charge transfer path of type-II heterojunction for photocatalytic hydrogen evolution. Appl. Catal. B Environ. 256, 117853.

Chen, J., Huang, Q., Huang, H., Mao, L., Liu, M., Zhang, X., Wei, Y., 2020. Recent progress and advances in the environmental applications of MXene related materials. Nanoscale 12, 3574–3592.

Chen, J., Yuan, X., Lyu, F., Zhong, Q., Hu, H., Pan, Q., Zhang, Q., 2019. Integrating MXene nanosheets with cobalt-tipped carbon nanotubes for an efficient oxygen reduction reaction. J. Mater. Chem. A 7, 1281–1286.

Cheng, Y., Awan, U., Ahmad, S., Tan, Z., 2021. How do technological innovation and fiscal decentralization affect the environment? A story of the fourth industrial revolution and sustainable growth. Technol. Forecast. Soc. Change 162, 120398.

Cormier, R., Elliott, M., 2017. Smart marine goals, targets and management–is SDG 14 operational or aspirational, is 'Life below Water'sinking or swimming? Mar. Pollut. Bull. 123, 28–33.

Dunne, J.A., Williams, R.J., Martinez, N.D., 2002. Network structure and biodiversity loss in food webs: robustness increases with connectance. Ecol. Lett. 5, 558–567.

Fu, J., Xu, Q., Low, J., Jiang, C., Yu, J., 2019. Ultrathin 2D/2D WO_3/g-C_3N_4 step-scheme H_2-production photocatalyst. Appl. Catal. B Environ. 243, 556–565.

Gita, S., Hussan, A., Choudhury, T., 2017. Impact of textile dyes waste on aquatic environments and its treatment. Environ. Ecol. 35, 2349–2353.

Hu, X., Wang, Y., Ling, Z., Song, H., Cai, Y., Li, Z., Zu, D., Li, C., 2021. Ternary g-C_3N_4/TiO_2/Ti_3C_2 MXene S-scheme heterojunction photocatalysts for NOx removal under visible light. Appl. Surf. Sci. 556, 149817.

Islam, T., Repon, M.R., Islam, T., Sarwar, Z., Rahman, M.M., 2023. Impact of textile dyes on health and ecosystem: a review of structure, causes, and potential solutions. Environ. Sci. Pollut. Control Ser. 30, 9207–9242.

Kane, A., Chafiq, L., Dalhatou, S., Bonnet, P., Nasr, M., Gaillard, N., Dikdim, J.M.D., Monier, G., Assadi, A.A., Zeghioud, H., 2022. g-C_3N_4/TiO2 S-scheme heterojunction photocatalyst with enhanced photocatalytic Carbamazepine degradation and mineralization. J. Photochem. Photobiol. Chem. 430, 113971.

Khan, W.U., Ahmed, S., Dhoble, Y., Madhav, S., 2022. A critical review of hazardous waste generation from textile industries and associated ecological impacts. J. Indian Chem. Soc., 100829

Kim, H., Franco, A.C., Sumaila, U.R., 2023. A selected review of impacts of ocean deoxygenation on fish and fisheries. Fishes 8, 316.

Kumar, A., Mittal, H., Nagar, R., Khanuja, M., 2022. The synergistic effect of acid-etched gC_3N_4 nanosheets and polyaniline nanofibers for the adsorption and photocatalytic degradation of textile dyes: a study of charge transfer mechanism and intermediate products. Materials Advances 3, 5325–5336.

Kumar, A., Singh, S., Khanuja, M., 2020. A comparative photocatalytic study of pure and acid-etched template free graphitic C_3N_4 on different dyes: an investigation on the influence of surface modifications. Mater. Chem. Phys. 243, 122402.

Kumawat, A.K., Nathawat, R., Rathore, S.S., Mukhopadhyay, A.K., 2021. Band gap tuning possibilities in vanadium oxide. Mater. Today: Proc. 43, 2939–2943.

Lee, E., VahidMohammadi, A., Prorok, B.C., Yoon, Y.S., Beidaghi, M., Kim, D.-J., 2017. Room temperature gas sensing of two-dimensional titanium carbide (MXene). ACS Appl. Mater. Interfaces 9, 37184–37190.

Lei, W., Zhou, T., Pang, X., Xue, S., Xu, Q., 2022. Low-dimensional MXenes as noble metal-free co-catalyst for solar-to-fuel production: progress and prospects. J. Mater. Sci. Technol. 114, 143–164.

Lim, H.-S., Choi, S.B., Kwon, H., Lim, J., Han, C.J., Oh, J.-M., Kim, J.W., 2021. Development of a highly flexible composite electrode comprised of Ti_3C_2-based MXene nanosheets and Ag nanoparticles. Electron. Mater. Lett. 17, 513–520.

Loeb, S.K., Alvarez, P.J., Brame, J.A., Cates, E.L., Choi, W., Crittenden, J., Dionysiou, D. D., Li, Q., Li-Puma, G., Quan, X., 2018. The Technology Horizon for Photocatalytic Water Treatment: Sunrise or Sunset? ACS Publications.

Maheshwari, K., Agrawal, M., Gupta, A., 2021. Dye pollution in water and wastewater. Novel Materials for Dye-Containing Wastewater Treatment, pp. 1–25.

Mani, S., Bharagava, R.N., 2018. Textile industry wastewater: environmental and health hazards and treatment approaches. In: Recent Advances in Environmental Management. CRC Press, pp. 47–69.

Mehra, S., Singh, M., Chadha, P., 2021. Adverse impact of textile dyes on the aquatic environment as well as on human beings. Toxicol. Int. 28, 165.
Mittal, H., Kumar, A., Sharma, D., Khanuja, M., 2024. Z-Scheme enabled 1D/2D nanocomposite of ZnO nanorods and functionalized g-C_3N_4 nanosheets for sustainable degradation of terephthalic acid. ChemSusChem, e202401408.
Pei, Y., Zhang, X., Hui, Z., Zhou, J., Huang, X., Sun, G., Huang, W., 2021. $Ti_3C_2T_X$ MXene for sensing applications: recent progress, design principles, and future perspectives. ACS Nano 15, 3996–4017.
Peng, Y., Deng, L., Zhang, P., Gao, X., Huang, S., Fang, S., Qin, T., Li, C., 2022. Tunable and broadband high-performance microwave absorption of $ZnFe_2O_4$ nanoparticles decorated $Ti_3C_2T_x$ MXene composites. J. Magn. Magn Mater. 541, 168544.
Ramzan, M., Raza, S.A., Usman, M., Sharma, G.D., Iqbal, H.A., 2022. Environmental cost of non-renewable energy and economic progress: ICT and financial development mitigate some burden? J. Clean. Prod. 333, 130066.
Roy Choudhury, A., 2014. Environmental Impacts of the Textile Industry and its Assessment through Life Cycle Assessment. Roadmap to Sustainable Textiles and Clothing: Environmental and Social Aspects of Textiles and Clothing Supply Chain, vol. 43, pp. 1–39.
Sadanandan, A., Thomas, S.A., Khan, M.E., Alomar, M.S., Pallavolu, M.R., Cherusseri, J., 2023. A critical review on two-dimensional $Ti_3C_2T_x$ MXenes for anti-corrosion coatings. Prog. Org. Coating 183, 107757.
Sadeghzadeh-Attar, A., 2020. Enhanced photocatalytic hydrogen evolution by novel Nb-doped SnO_2/V_2O_5 heteronanostructures under visible light with simultaneous basic red 46 dye degradation. Journal of Asian Ceramic Societies 8, 662–676.
Sharma, K., Hasija, V., Patial, S., Singh, P., Nguyen, V.-H., Nadda, A.K., Thakur, S., Nguyen-Tri, P., Nguyen, C.C., Kim, S.Y., 2023. Recent progress on MXenes and MOFs hybrids: structure, synthetic strategies and catalytic water splitting. Int. J. Hydrogen Energy 48, 6560–6574.
Sharma, J., Sharma, S., Soni, V., 2021. Classification and impact of synthetic textile dyes on Aquatic Flora: a review. Regional Studies in Marine Science 45, 101802.
Sivasankarapillai, V.S., Sharma, T.S.K., Wabaidur, K.-Y.H.S.M., Angaiah, S., Dhanusuraman, R., 2022. MXene based sensing materials: current status and future perspectives. ES Energy & Environment 15, 4–14.
Soni, V., Singh, P., Quang, H.H.P., Khan, A.A.P., Bajpai, A., Van Le, Q., Thakur, V.K., Thakur, S., Nguyen, V.-H., Raizada, P., 2022. Emerging architecture titanium carbide ($Ti_3C_2T_x$) MXene based photocatalyst toward degradation of hazardous pollutants: recent progress and perspectives. Chemosphere 293, 133541.
Spasiano, D., Marotta, R., Malato, S., Fernandez-Ibanez, P., Di Somma, I., 2015. Solar photocatalysis: materials, reactors, some commercial, and pre-industrialized applications. A comprehensive approach. Appl. Catal. B Environ. 170, 90–123.
Tahir, T., Chaudhary, K., Warsi, M.F., Saif, M.S., Alsafari, I.A., Shakir, I., Agboola, P.O., Haider, S., Zulfiqar, S., 2022. Synthesis of sponge like Gd^{3+} doped vanadium oxide/2D MXene composites for improved degradation of industrial effluents and pathogens. Ceram. Int. 48, 1969–1980.
Tawalbeh, M., Mohammed, S., Al-Othman, A., Yusuf, M., Mofijur, M., Kamyab, H., 2023. MXenes and MXene-based materials for removal of pharmaceutical compounds from wastewater: critical review. Environ. Res. 228, 115919.
Tkaczyk, A., Mitrowska, K., Posyniak, A., 2020. Synthetic organic dyes as contaminants of the aquatic environment and their implications for ecosystems: a review. Sci. Total Environ. 717, 137222.
Tyagi, N., Ashraf, W., Mittal, H., Fatima, T., Khanuja, M., Singh, M.K., 2023a. A facile synthesis of ternary hybrid nanocomposite of WS_2/ZnO/PPy: an efficient photocatalyst for the degradation of chromium hexavalent. Dyes Pigments 210, 110998.
Tyagi, N., Bhardwaj, V., Moka, S., Singh, M.K., Khanuja, M., Sharma, G., 2024a. An overview on synthesis of MXene and MXene based nanocomposites for supercapacitors. Mater. Today Commun. 41, 110223.
Tyagi, N., Sharma, G., Ashraf, W., Singh, S., Singh, M.K., Khanuja, M., 2024b. Review on recent advancements of 2D MXene-based nanostructures on different possible approaches for wastewater treatment. Chem. Phys. Lett. 485, 141320.
Tyagi, N., Sharma, G., Kumar, D., Neelratan, P.P., Sharma, D., Khanuja, M., Singh, M.K., Singh, V., Kaushik, A., Sharma, S.K., 2023b. 2D-MXenes to tackle wastewater: from purification to SERS-based sensing. Coord. Chem. Rev. 496, 215394.
Tyagi, N., Singh, M.K., Khanuja, M., 2023c. Synergistic effect of polypyrrole modified WS_2 nanosheets on visible light assisted catalysis for the removal of chromium (VI) and humic acid. Mater. Res. Bull. 163, 112216.
Tyagi, N., Singh, M.K., Khanuja, M., 2023d. WS_2 nanosheets modified via ZnO nanorods (2D/1D) nanocomposite: an efficient photocatalyst for the removal of Cr (VI), humic acid and textile dyes from wastewater. Ceram. Int. 49, 34447–34460.
Tyagi, N., Singh, M.K., Moka, S., Khanuja, M., 2024c. Facile synthesis of MXene from MAX phase via Hydrothermal method using a mild etchant. Hybrid Advances 7, 100285.
Vadrot, A.B., 2023. Protecting life below water: competing normative, economic and epistemic orders (SDG 14). The Environment in Global Sustainability Governance. Bristol University Press, pp. 72–95.
Wang, J., Zhang, Q., Deng, F., Luo, X., Dionysiou, D.D., 2020. Rapid toxicity elimination of organic pollutants by the photocatalysis of environment-friendly and magnetically recoverable step-scheme $SnFe_2O_4/ZnFe_2O_4$ nano-heterojunctions. Chem. Eng. J. 379, 122264.
Wang, Y., Zheng, W., Zhang, P., Tian, W., Chen, J., Sun, Z., 2019. Preparation of (V_x, Ti_{1-x})2C MXenes and their performance as anode materials for LIBs. J. Mater. Sci. 54, 11991–11999.
Würth, C., Grabolle, M., Pauli, J., Spieles, M., Resch-Genger, U., 2013. Relative and absolute determination of fluorescence quantum yields of transparent samples. Nat. Protoc. 8, 1535–1550.
Xavier, J.R., 2021. High protection performance of vanadium pentoxide-embedded polyfuran/epoxy coatings on mild steel. Polym. Bull. 78, 5713–5739.
Xu, Q., Zhang, L., Yu, J., Wageh, S., Al-Ghamdi, A.A., Jaroniec, M., 2018. Direct Z-scheme photocatalysts: principles, synthesis, and applications. Mater. Today 21, 1042–1063.
Xue, W., Sun, H., Hu, X., Bai, X., Fan, J., Liu, E., 2022. UV-VIS-NIR-induced extraordinary H_2 evolution over $W_{18}O_{49}$/CdO. 5ZnO. 5S: surface plasmon effect coupled with S-scheme charge transfer. Chin. J. Catal. 43, 234–245.
Yoon, T.P., Ischay, M.A., Du, J., 2010. Visible light photocatalysis as a greener approach to photochemical synthesis. Nat. Chem. 2, 527–532.
Yu, M., Liang, H., Zhan, R., Xu, L., Niu, J., 2021. Sm-doped g-C_3N_4/Ti_3C_2 MXene heterojunction for visible-light photocatalytic degradation of ciprofloxacin. Chin. Chem. Lett. 32, 2155–2158.
Zehra, F., Tyagi, N., Mittal, H., Singh, M.K., Khanuja, M., 2023. Synthesis and comparative study of Zeolite imidazole framework for the removal of textile dyes from wastewater. Mater. Today: Proc.